Nanoscale

Dynamic Article Links ▶

ARTICLE TYPE

Shape-Controlled Synthesis of Nanopyramids and Nanoprisms of Nickel Sulfide (Ni3S4)[†]

Qingsheng Liu,[a, b‡] Agustín Díaz,[a‡] Andrey Prosvirin,[a] Zhiping Luo,[c,d] and James D. Batteas*[a]

Two different nickel precursors ($NiCl_2$ or $Ni(CH_3COCH_2COCH_3)_2$) in the presence of 1-dodecanethiol and a mixture of oleylamine and oleic acid were used for a one-pot colloidal synthesis to produce high purity Ni_3S_4 nanoparticles with controlled shapes in high yields and narrow size distributions. By simply changing the nickel precursors, the shape of Ni_3S_4 nanocrystals can be readily tuned from triangular
10 nanoprisms to tetrahedrons (nanopyramids). The produced nanocrystals were characterized by transmission electron microscopy (TEM), energy-dispersive X-ray spectroscopy (EDS), X-ray powder diffraction, selected area electron diffraction, ultraviolet–visible spectroscopy and superconducting quantum interference device (SQUID). TEM tomography (3D-TEM) was employed to determine details of the particle shapes. SQUID measurements confirmed that particle shape and domain size could
15 dramatically impact their magnet properties, where tetrahedral nanopyramids of Ni_3S_4 nanoparticles showed ferromagnetic properties while the Ni_3S_4 nanoprisms showed random antiferromagnetic interactions between magnetic centers.

Introduction

The shape controlled synthesis of nanocrystals has gained
20 increasing attention, as many of their physical and chemical properties are found to be highly shape dependent. By tuning the shape, surface morphology, bounding facets, step edges and kink sites, as well as the volume to bulk ratio of the nanocrystals, the catalytic activity and selectivity of metal catalysts can be
25 significantly enhanced.[1-5] Moreover, the shape control of nanocrystals is a heavily researched area due to the potential applications in fields spanning from optical devices,[6] optoelectronic devices,[7, 8] solar cell,[8, 9] electronic circuits,[7, 10] photoconductivity,[7] lasing,[11, 12] and sensing[13, 14].
30 Synthesis of nickel sulfides with controlled morphology is of great interest due to their potential applications in rechargeable lithium batteries[15] and catalysis,[16, 17] especially for hydrodenitrogenation and hydrodesulfurization processes. Ni_3S_4 has attracted much less attention compared to other binary nickel
35 sulfides, such as NiS, Ni_3S_2, NiS_2, Ni_9S_8, and Ni_7S_6, due to the synthetic challenges in obtaining the single phase Ni_3S_4.[18-22] Ni_3S_4 has a cubic spinel structure and is found in nature as the mineral polydymite.[23] Traditionally, Ni_3S_4 along with NiS and NiS_2 impurities, has been synthesized through solid state
40 reactions between Ni and S, NiS and S, or NiS and NiS_2 at 200 – 300 °C for up to 8 months, due to their instability at higher temperatures (360 °C).[24, 25] Subsequently many efforts have been attempted in order to obtain the single-phase Ni_3S_4 efficiently in laboratories. Manthiram and coworkers successfully synthesized
45 Ni_3S_4 at room temperature using an aqueous nickel chloride in a

sodium dithionite solution.[26, 27] Ni_3S_4 has been also obtained by colloidal processes with elemental sulfur as precursor in oleylamine at high temperature (180 °C).[28, 29] Alternatively, Ni_3S_4 has been found to appear as a byproduct in the solventless
50 synthesis of rhombohedral NiS nanorods and triangular nanoprisms[20] or under hydrothermal conditions.[30, 31] However, the synthetic approaches mentioned above produced either poor crystallinity or irregular shaped particles. Through selective control of the reaction conditions, such as which Ni precursor is
55 used or which capping agents are employed, it is possible to obtain single phases of Ni_3S_4. Recently Tuna and coworkers reported the synthesis of Ni_3S_4 nanoparticles with different shapes by thermolysis using a single-source Ni precursor ([bis(1,1,5,5-tetra-isopropyl-2-thiobiuret) nickel(II)]) in the
60 presence of oleylamine, octadecene, or dodecanethiol.[32] We have also explored similar phenomena with size and shape tunable metal nanostructures.[33]

In response to these considerable challenges, here we demonstrate a facile approach to the synthesis of Ni_3S_4
65 nanoparticles with high crystallinity, narrow size distributions and controlled shapes, dictated by the choices of Ni precursor and capping agents.

Experimental section

Instrumentation and materials

70 The powder X-ray diffraction (PXRD) patterns were recorded on a Bruker Advance D8 X-ray diffractometer using Cu Kα radiation. Transmission electron microscopy (TEM) images were

Nanoscale Accepted Manuscript

taken on a JEOL JEM-2010 TEM operating at 200 kV. The TEM samples were prepared by placing one drop of hexane suspension onto a carbon coated Cu grid and allowing it to dry in air. The energy-dispersive spectroscopy (EDS) measurement was

5 performed using an Oxford Instruments EDS detector with INCA energy platform. Magnetic measurements were performed on a Quantum Design SQUID magnetometer MPMS-XL in an applied field of 1000 Oe in the 2–300 K temperature range. All reagents were purchased from Aldrich and used without further

10 purification.

General Synthesis of the Ni₃S₄ nanoparticles

The nanoparticles were synthesized using standard Schlenk line techniques under an inert argon atmosphere. In a typical synthesis 200 mmoles of the nickel complex ($NiCl_2 \cdot 6H_2O$ or

15 $Ni(acac)_2(H_2O)_2$, (acac = $CH_3COCH_2COCH_3$)), 105 mg of 1,2-hexadecanediol, 0.2 mL of oleic acid, 1.2 mL of oleylamine (70%) were mixed together with 5.0 mL of 1-octadecene (90%) in a 100 mL three-neck round-bottom flask. These conditions were varied to produce several other nanoparticles according to

20 Table 1 in the manuscript and Table S1† in the electronic supplementary information (ESI). The flask was purged with Ar, heated to 90 °C and then 0.45 mL of 1-dodecanethiol was added to the reaction through a syringe. The reaction was heated to 120 °C for 40 min, and then heated up to 225 °C at a rate of 20

25 °C/min. After 1 min, the black-colored solution was cooled to room temperature. The nanocrystals were washed with abundant hexanes and acetone by centrifugation. *Note: nickel sulphides are known carcinogens and should be handled with care.*

Results and discussion

30 Ni₃S₄ nanoparticles were prepared through a colloidal synthesis process with $NiCl_2 \cdot 6H_2O$, or $Ni(acac)_2(H_2O)_2$, and 1-dodecanethiol as precursors. The reaction was typically carried out in 1-octadecene with oleylamine and oleic acid as the capping ligands. When using $NiCl_2 \cdot 6H_2O$ as the Ni precursor, Ni₃S₄

35 nanoprisms were obtained (Fig. 1a). By replacing the Ni precursor with $Ni(acac)_2(H_2O)_2$ (from now on $Ni(acac)_2$) however, while keeping all the synthetic conditions identical to the Ni₃S₄ nanoprisms preparation, tetrahedral nanocrystals (nanopyramids) are produced (Fig. 1b).

40 The nanoprism dimensions were found to be 38.1 ± 5.0 nm (in length) × 9.0 ± 1.4 nm (in width), with the size distributions determined calculations of *ca.* 300 nanoprisms. Corresponding histograms are shown in Fig. 1c and Fig. 1d, respectively, confirming the uniformity of Ni₃S₄ nanoprisms in both length and

45 width. When examined over much larger sampling area, assembly of the Ni₃S₄ nanoprisms could be observed, indicating a short-ordered arrangement of nanoprisms on the TEM grid (Fig. S1†).
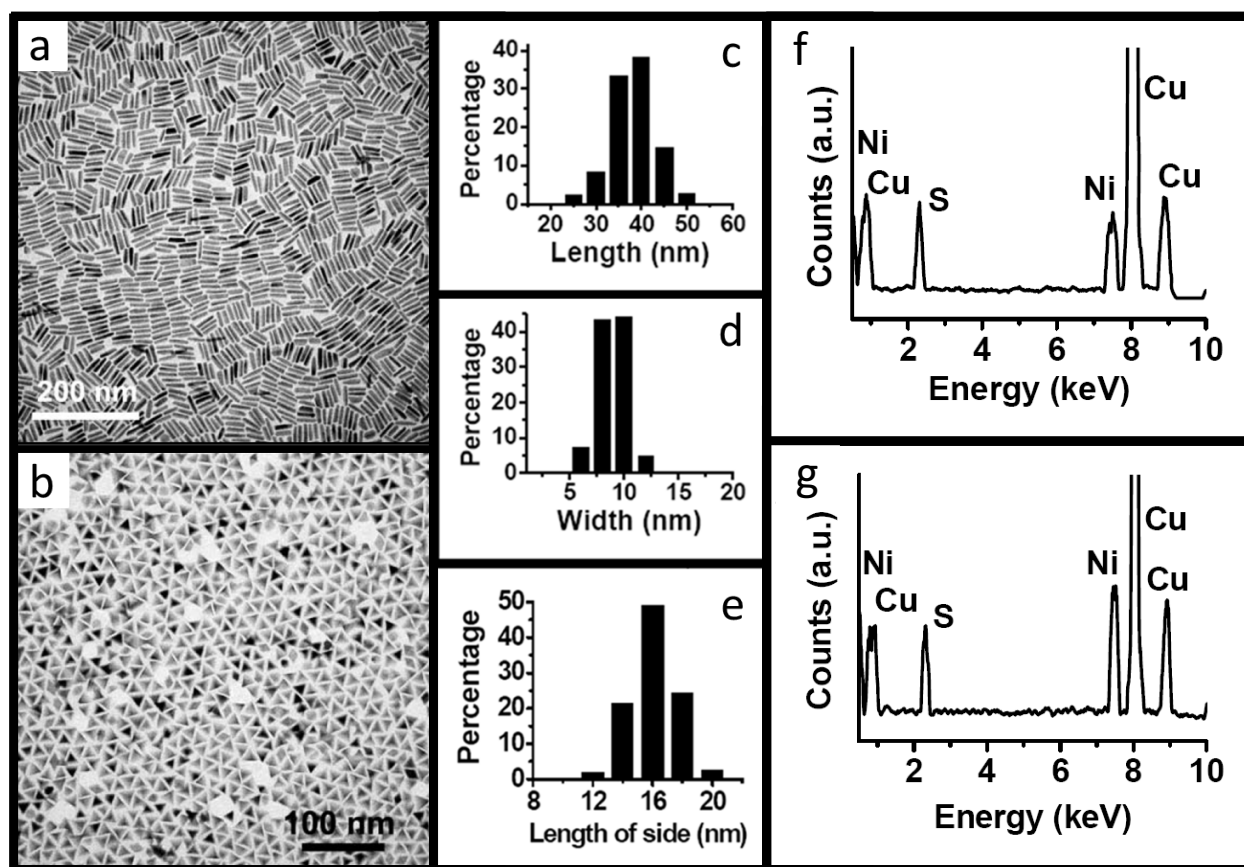
Fig. 1 Nanoparticles morphological characterization: a) TEM image of the Ni₃S₄ nanoprism synthesized using NiCl₂ as the Ni precursor; b) TEM image of

50 the Ni₃S₄ tetrahedron (nanopyramids) synthesized using Ni(acac)₂ as the Ni precursor; c and d) length (c) and width (d) distribution for the Ni₃S₄ nanoprisms (40 nm x 10 nm); e) length distribution of the edges for the Ni₃S₄ tetrahedrons (16 nm); f) EDS of the Ni₃S₄ nanoprism; g) EDS of the Ni₃S₄ tetrahedral nanopyramids.

Nanoscale

Nanoscale

ARTICLE TYPE

On the other hand, the Ni_3S_4 tetrahedral nanopyramid crystals have an average edge length of 16.0 ± 1.6 nm (Fig. 1b). As seen in Fig. 1b and Fig. S2† more than 98% of the nanoparticles are triangular with identical sides, while the remaining 2% consisted

5 of diamond and spherical shape particles. It is important to note that the prism shape particles were never found when $Ni(acac)_2$ was used as Ni precursor. The side length of the equilateral triangle distribution histogram was determined from measurements of more than 300 tetrahedral Ni_3S_4 nanoparticles

10 (Fig. 1e) and as with the prisms, showed a very narrow size distribution of Ni_3S_4. The chemical composition of the nanocrystals was determined from the energy-dispersive X-ray spectroscopy (EDS). The EDS for the Ni_3S_4 nanoprism (Fig. 1f) shows a Ni:S atomic ratio of *ca.* 45:55 (0.82), which is close to

15 the nominal Ni:S ratio of 0.75 in Ni_3S_4. For the Ni_3S_4 nanopyramids, the EDS analysis (Fig. 1g) showed a very similar spectrum to that obtained from the Ni_3S_4 nanoprism (Fig. 1f), with a Ni:S atomic ratio also of *ca.* 45:55 (0.82).
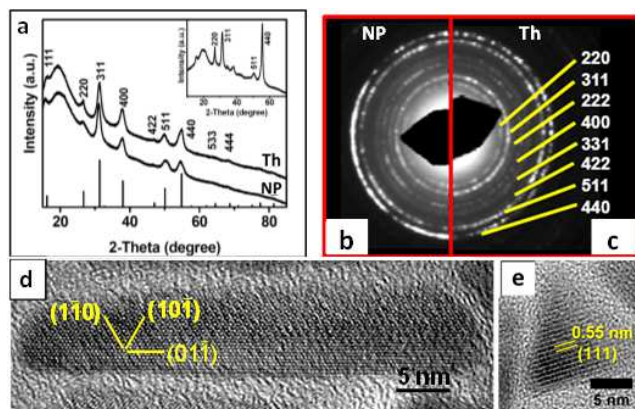

20 **Fig. 2** Nanoparticles crystallographic characterization: a) X-ray powder diffraction for the Ni_3S_4 nanoprisms (NP) and tetrahedral nanopyramids (Th), inset: X-ray powder diffraction of the Ni_3S_4 nanoparticles avoiding preferential orientations; b and c) SAED for the Ni_3S_4 NPs and Ths; d) HR-TEM images of a single Ni_3S_4 nanoprism crystal showing the (1-10),

25 (10-1) and (01-1) planes; e) HR-TEM images of two typical single nanopyramids tetrahedrons showing the interplanar lattice distances for the (111) plane.

Detailed structural characterization of the nanocrystals was obtained from X-ray diffraction (XRD) and selected area electron

30 diffraction (SAED) patterns (Fig. 2). A typical powder XRD pattern for the Ni_3S_4 nanoprisms and nanopyramids is shown in Fig. 2a. The XRD diffractograms, for both particles, shows a typical pattern of a spinel cubic structure with peaks position that are in agreement with those of face-centered cubic (fcc) Ni_3S_4

35 (JCPDS 01-076-1813 marked as lines in the XRD). Its lattice parameter was refined to 0.9444 nm using the Pawley refinement algorithm.[34] No other peaks from impurities such as NiS, Ni or NiO were detected. The clear diffraction ring of the SEAD patterns for both particles (Fig. 2b and 2c) reveals the highly

40 crystalline nature of the Ni_3S_4 nanoparticles. The distances between the diffraction rings calculated are the same for both Ni_3S_4 nanocrystals. All of the *d*-spacings calculated perfectly matched the fcc Ni_3S_4 phase (JCPDS 01-076-1813), in agreement with the XRD data.

45 The HR-TEM image of the Ni_3S_4 nanoprisms shows that they appear to be single crystals (Fig. 2d). Its horizontal facet is parallel to (01-1), indicating the facets of the nanoprism are {011} type of the cubic crystal which can form regular triangular shape along the <111> direction. The {011} type prism facets

50 appeared in other systems.[35] HR-TEM image of a typical single nanopyramid is shown in Fig. 2e. Its lattices are parallel to the facet, with interplanar distance of 0.55 nm, matching well with the plane spacing of (111) of the cubic Ni_3S_4. The facets of the nanopyramids are therefore {111} type, consistent with the

55 literature.[36] These results confirmed that the triangle shape particles made from Ni(acac)2 have the same composition with Ni_3S_4 and the same crystal structure than the Ni_3S_4 nanoprisms.

To further elucidate their morphology, the Ni_3S_4 nanocrystals were analyzed by electron tomography, a technique used to

60 obtain three-dimensional (3D TEM) volume information. This technique has mainly been used in the characterization of biomaterials, but has recently been applied in materials science to characterize different 3D nanostructures.[37, 38] A regular TEM image containing several tens of Ni_3S_4 nanoprisms is shown in

65 Fig. 3a, from which an aggregation of "rod" like Ni_3S_4 with average length about 50 nm and width of ~12 nm is observed. It seems that most of the Ni_3S_4 "rods" are self-assembled on the TEM grid with several stacking on the second layer. However, using 3D-TEM reconstruction technique, it is found that all the

70 Ni_3S_4 particles in this area actually consist of two sections. Most of them are located on the top of the TEM grid and the others are under the polymer film of the grid. Fig. 3b shows a reconstructed 3D tomographic cross-section perpendicular to the image plane (or side view). As a comparison, a model with two simulated

75 prisms exhibiting cross sections is inserted with each Ni_3S_4 "rod" ending with a triangular cross-section. Moreover, the lengths of the triangle's three sides are almost the same at ~ 12 nm, which is close to the width of the "rod" measured by regular TEM. Interestingly, two triangles for most adjacent "rods" are standing

80 oppositely on the TEM film (marked rectangle), likely due to strong face-to-face interactions.

Three typical cross sections parallel to the imaging plane through a 3D reconstruction are shown in Fig. 3c to 3e; a cartoon demonstrating the corresponding cross planes of prisms is given

85 in each figure. Fig. 3c show the cross-sectional view near the top of the reconstructed volume. The width of the bright "rod" (marked area with a pink square on Fig. 3c) is ca. 4 nm. The width of the "rod" increased to about 8.2 nm at middle cross-section plane (Fig. 3d) and about 11.5 nm near the bottom cross-

90 section plane (Fig. 3e). Based on these results, it can be deduced that the edge length of the nanoprism is of ca. 12 nm. Moreover,
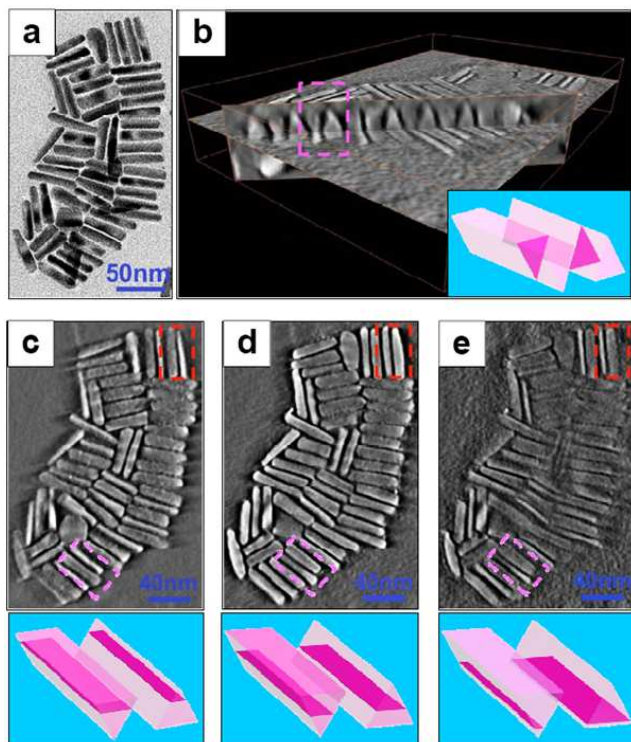
Fig. 3 3D-TEM images of the Ni3S4 nanoprisms: a) TEM image of the Ni3S4 nanoprisms; b) reconstructed 3D tomographic cross-section image perpendicular to the image plane; (c-e) cross-section planes from at different height of the reconstructed volume. Insets: schematic representation of the nanoprisms enclosed in the pink rectangles in the images, showing their variable cross sections as a function of height.

it is noted that for the adjacent nickel sulfide nanoprism, in both marked areas, an opposite trend is observed, where the width of the "rod" decreases as the numerical cross-section plane increased. A movie with the complete 3D reconstruction of the nanoprism can be found in the ESI denoted: Movie #1†. The combination of TEM results and tomographic analysis shows that the Ni_3S_4 "rods" are actually triangular nanoprisms, with side faces enclosed by {110} facets and preferentially grows through the <111> direction. Two adjacent nanoprisms are lying reversely on TEM grid in an energetically favored way due to the maximized van der Waals interactions arising from the face-to-face orientation.

The morphology of Ni_3S_4 nanopyramids was also examined with 3D-TEM. As shown in Fig. 4a, a regular TEM image exhibiting a small area of "triangle" shape Ni_3S_4 nanoparticles with average side length of ~16 nm was observed. The observed "triangle" can arise as a projection from a three dimensional particle with possible shapes such as triangular prisms (standing), plates, or a tetrahedral pyramid. Three typical cross-section planes through the 3D reconstruction parallel to imaging plane are shown from Fig. 4b to 4d and cartoons demonstrating the corresponding cross planes of a pyramid viewed from a perpendicular plane to the imaging plane are given in corresponding insets. Fig. 4a shows the cross-section plane near the top of the reconstructed volume (ESI denoted: Movie #2†). Apparently most shapes in this plane are equilateral triangles with side length of ~15.5 nm, which is analogous to about 97% of an equilateral triangle with side length
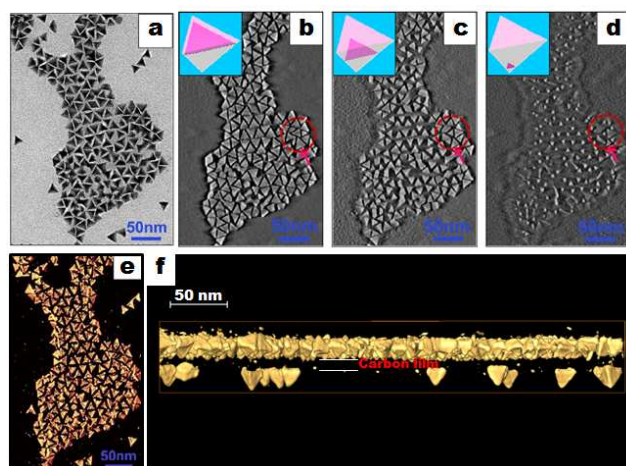

Fig. 4 3D-TEM images of the Ni_3S_4 nanopyramids: a) TEM image of the Ni_3S_4 tetrahedral nanopyramids; b, c, and d) TEM images of the reconstructed volume cross-section plane for the Ni_3S_4 nanopyramids at top (b), middle (c), and bottom (d) of the 3D voxel matrix of the selected nanopyramids; e and f) top view (e) and side view (f) of the reconstructed 3D tomographic image for the nanopyramids. Insets: schematic representation of the nanopyramids enclosed in the pink rectangles in the images.

of 16 nm. Fig. 4b shows a typical equilateral triangle nanoparticle pointed by a red arrow.

At a cross-section plane at the middle height of the reconstructed volume, equilateral triangular shapes are at the same location (pointed by red arrow in Fig. 4c) but with smaller side length (about 10.5 nm), approximately a 66% of the equilateral triangle with side length of 16 nm. A similar trend is observed for most shapes at this plane compared to those in Fig. 4b.As the viewing plane further moves down, the equilateral triangle shown at the same location is even smaller with side length of ~ 6 nm (about 37% of an equilateral triangle with side length of 16 nm). This is also a representative shape at this plane. The proportional variations of equilateral triangle in size at different cross-section planes confirmed that the Ni_3S_4 particle synthesized have a tetrahedral pyramids shape. Interestingly, the decrease in size for most of the nanopyramids as the cross-section planes come closer to the TEM grid indicates that the Ni_3S_4 pyramids are standing on the tip over the grid. Fig. 4e shows the 3D reconstruction top view where the bottoms of the nanopyramids are observed in most of the cases, and Fig. 4f is the side view of the assembly showing assembled nanoparticles standing on the carbon film on their tips, while few isolated nanoparticles on the backside of the carbon film standing on their faces. We also checked several different particles on the grid and found that in most cases the Ni_3S_4 nanopyramids adopted the same position, standing on the TEM grid film with the exception of some small particles marked with red circles, where 4 adjacent Ni_3S_4 nanopyramids assembly conversely. This phenomenon (tip down standing) is energetically unfavorable, probably due to the strong interactions between nanoparticle tips, as observed in nanoctahedral system.[39]

In order to understand the growth mechanism of the Ni_3S_4 nanoparticles, under our one-pot synthesis procedure, we performed a number of systematic experiments varying the reactions conditions to determine the role of each ingredient in our approach. We found that the size of the nanoprism can be

Nanoscale

ARTICLE TYPE

Table 1 Summary of reaction conditions to obtain Ni_3S_4 nanoprisms of different sizes.

Sample*	Length (nm)	Width (nm)	Aspect Ratio[a]	Ni:OLM[b] Molar ratio	Ni:OLA[c] Molar ratio	Ni:DDT[d] Molar ratio	Comments
Typical	*38.1*	*9.1*	*4.2*	*53*	*307*	*104*	
1	-	-	-	53	307	39	No product
2	39.7	9.4	4.2	53	307	78	
3	38.7	9.1	4.2	53	307	311	
4	-	-	-	53	307	777	Mixture of irregular shapes
5	-	-	-	53	307	-	No product
6	32.2	8.4	3.8	53	-	104	
7	42.7	10.4	4.1	53	154	104	
8	47.0	10.1	4.6	53	102	104	
9	52.7	13.0	4.0	53	102	104	Short reaction time (5 min)
10	35.8	9.3	3.8	53	102	104	205 °C, low yield
11	38.8	9.2	4.2	80	307	104	
12	40.2	9.9	4.1	160	307	104	
13	43.3	9.6	4.5	18	123	35	Low Ni concentration
14	23.4	6.8	3.4	160	877	311	High Ni concentration

[a] aspect ratio of length/width; molar ratios of [b] Ni:oleylamine; [c] Ni:oleic acid; [d] Ni:1-dodecanethiol.

tuned by varying the reaction conditions, such as capping ligand ratios, reaction time and reactant concentrations. Controlling the
5 reaction parameters, the length of nanoprism can be tuned from 23 nm to 52 nm and the width can be tuned from 7 nm to 13 nm approximately, while maintaining the similar aspect ratio of about 4.

Table 1 summarizes factors that affected the size of Ni_3S_4
10 nanoprisms. From Table 1 it can be clearly observed that the concentration of 1-dodecanethiol in the synthetic mixture influences the formation of the Ni_3S_4 nanoparticles. As seen in sample #5, there is no formation of Ni_3S_4 nanoparticles in the absence of 1-dodecanethiol, indicating the important role of
15 dodecanethiol, providing the sulfur precursor for the Ni_3S_4 nanoparticles formation. However, small amounts of 1-dodecanethiol (770:1 molar ratio) do not affect control of the shape of the nanoparticles, as was the case with sample #4. On the other hand, too high concentration of 1-dodecanethiol (35:1
20 molar ratio), as in sample 13, may retard the formation of Ni_3S_4, due to the fact that 1-dodecanethiol also acts as a capping ligand, interacting strongly with the Ni atoms inhibiting the Ni-S aggregation. The strong interaction between 1-dodecanethiol and the Ni atoms can also be demonstrated by the UV-vis absorption
25 in supplementary information (Fig. S3†). In order to get uniform Ni_3S_4 nanoprisms, it is necessary to use 1-dodecanethiol in molar ratios (Ni:1-dodecanethiol) between 311 and 777. The concentration of 1-dodecanethiol has no apparent effect on the size of the Ni_3S_4 nanoprisms within this range.
30 Another important factor to control the shape of the particles is the concentration of acid used in the synthesis. When the concentration of oleylamine (OLM) was kept constant with a Ni:OLM molar ratio of 53 in the reaction mixture and the

concentration of oleic acid (OLA) is increased, the obtained
35 particles shown an increase in the length of the Ni_3S_4 nanoprisms from 32.2 nm to 47.0 nm (samples 6-10). However, further increases of oleic acid concentration on the reaction mixture accelerate the aggregation of the Ni_3S_4 nanoprisms formed, resulting in a broad distribution of particles sizes. On the other
40 hand, other than improve the solubility of $NiCl_2·6H_2O$ into the synthesis mixture, oleylamine has no significant influence on the growth of the Ni_3S_4 nanoprisms (Table 1). Nevertheless, the reaction temperature in which the reaction takes place is an important factor that influences the yield of the final product,
45 where similar length and width of nanoprisms can be obtained at 205 °C.

Longer reaction times produced bigger nanoprisms with similar aspect ratios, but the final products were hard to disperse in organic solvents. Lower concentration of reactants resulted in
50 smaller nanoprisms, for example, Ni_3S_4 nanoprisms with average length of 23.4 nm and width of 6.8 nm were obtained with one third of the reactant concentration (sample 14). Conversely, higher concentration of reactant do not produces bigger nanoprisms.
55 Contrary to the formation of Ni_3S_4 nanoprisms, the yield of Ni_3S_4 nanopyramids was significantly affected by the concentration of oleylamine and oleic acid in the reaction mixture. The factors affecting the size and shape of the nanoparticles are summarized in Table SI-1†. From Table SI-1† it
60 can be deduced that the presence of both oleylamine and oleic acid are required to obtain high yield Ni_3S_4 tetrahedron. Lower oleylamine concentration will result in a low yield of product. However, with only oleylamine as the capping ligand, the final product was only related to reaction time. A mixture of

Nanoscale Accepted Manuscript

nanospheres, pyramids and nanorods with average length about 60 nm and diameter about 4 nm was obtained over a 5 minute reaction period. As the reaction proceeds past 30 minutes, nanowires with lengths of more than several hundred nanometers and irregular shapes were formed as the final product. Without oleylamine, the final product had a broad size distribution of nanobars with an average length of 17.2 nm and 6.5 nm of width. The solvents have an effect on the formation of tetrahedral nanopyramids, where relatively bigger sizes of nanoparticles were formed in octadecene (ODE) than in benzyl ether (BE).

In general, with nickel chloride as the precursor the concentration of oleylamine and oleic acid have no effect on the shape of the final product, producing triangular prisms as the only product. However, the concentration of oleylamine and oleic acid did have an effect on the particle shape when $Ni(acac)_2$ was used as precursor, obtaining shapes that varies from tetrahedral pyramids, nanowires, nanorods, to butterflies. Based on these, it is concluded that the aquo ligands play a critical role in the formation of the Ni_3S_4 nanoprism. Fig. S3† shows the UV-vis spectra of $NiCl_2$ and $Ni(acac)_2$ in the presence of the capping ligands in hexanes at 120 °C. It is obviously seen that the $Ni(acac)_2$ and the oleylamine can form a stable complex, probably the octahedral $(Ni(acac)_2(thiol)_2$ complex, with a strong absorption centered at 305 nm (Fig. S3b†). In comparison, no peaks can be found in this range when $NiCl_2$ and oleylamine are mixed (Fig. S3a†). The amine group of the oleylamine is too hard, compared to the aquo ligands, to form the $Ni(H_2O)_{6-x}(oleylamine)_x$ complex, which is crucial for the case of the borderline Ni^{2+} metal in the hard soft acid base theory. When oleic acid and dodecanethiol were later introduced to the solution mixture, with $NiCl_2$ as precursor, three new absorptions bands at 335 nm, 410 nm, and 525 nm appeared, which is characteristic of the formation of complex between the thiol (dodecanethiol) and the Ni^{2+} $(Ni(thiol)_2)$ displacing the aquo ligands, due to the soft base character of the thiol. In the case of $Ni(acac)_2$ as the precursor, two new peaks centered at 410 nm and 525 nm appeared and the peak at 305 nm becomes broad, suggesting that the Ni-oleylamine complex is no longer present and the formation of a new Ni-dodecanethiol complex is formed.

Herein, it is suggested that the presence of aquo ligands may prevent the interaction of oleylamine with the Ni atoms. In other words, the function of the oleylamine in the Ni-dodecanthiol-oleylmine-oleic acid system is just to improve the solubility of $NiCl_2$ and its concentration has no effect on the formation of the Ni_3S_4 nanoprism, which is consist with the experimental results (Table 1). It is worth noting that in the absence of oleylamine, with $Ni(acac)_2$ as the precursor, the system shows the same UV-vis spectrum compared with $NiCl_2$ as precursor (Fig S3†). In this case only Ni_3S_4 prisms were observed indicating the oleic acid probably adsorbed on the *110* facets side and retards the quick growth in these three faces to form a prism. Consequently the concentration of oleic acid in solution will affect the aspect ratio of the nanoprism, where higher concentration of oleic acid will result in relatively slower growth in width of the prism due to the enclosed three side faces of the *110* facets of the prism. The aspect ratio of the nanoparticles increased from 3.8 to 4.6 when the amount of oleic acid was increased in the reaction mixture. Moreover, it should be noted that the Ni_3S_4 nanoprisms were still

the final product in the absence of oleic acid while using $NiCl_2$ as the precursor.

Based on this, the only possible factor influencing the product shape is the chloride ions. In theory, the size of Cl⁻ is about 0.167 nm, which is very close to the Ni_3S_4 interlunar spacing of the (440) face (0.1672 nm). This similarity makes it possible for binding of the chloride ions to the (440) facets of the Ni_3S_4 nanoparticles, thus favoring the formation of the Ni_3S_4 nanoprism enclosed by the (110) facets. Based on these results, it is deduced that the concentration of chloride ions will affect the aspect ratio of the prism, meaning that the lowest the chloride concentration will result in the formation of Ni_3S_4 prism with smaller aspect ratio. Therefore, a control experiment was designed using a mixture of $NiCl_2$ and $Ni(acac)_2$ (1:1) as Ni precursor. The reaction was carried out under standard reaction conditions for producing the nanoprisms at *ca.* 100% yield. The average dimensions for the obtained nanoprism under these conditions are 22.4 nm (in length) × 7.3 nm (in width), which translate to an aspect ratio of *ca.* 3.1, significantly smaller than the standard ratio of 4.2 obtained under standard conditions. This result confirmed our hypothesis on the role of the chloride ions in the growth mechanism of the nanoparticles and that at lower chloride concentrations smaller aspect ratio Ni_3S_4 nanoprism will been produced.

The magnetic behavior of the obtained nanoparticles was quite interesting and is illustrated in Fig. 5. The nanoprism and nanopyramids exhibit room-temperature χT values of 2.57 and 3.8 emu·g⁻¹ K, respectively. Upon cooling, the χT values of sample nanoprism decrease indicating random antiferromagnetic interactions between magnetic centers (Fig. 5a). In accord with this assumption is the fact that the temperature dependences are well described to the Curie-Weiss law leading to a negative Weiss constant θ of -50 K and C = 3 emu·g⁻¹ K. After a broad minimum at about 30 K the χT increases to a maximum at about 11 K and then it decreases again (Fig. 5a). In the case of sample nanopyramids, however, the χT magnitude gradually increases to a broad maximum at ~ 12 K and then it decreases again (Fig. 5b). A treatment in terms of the Curie-Weiss law leads to positive Weiss constants θ of +20 K and C = 3.55 emu·g⁻¹ K, characteristic of a ferromagnetic material.

The difference of the magnetic behavior between the nanoprisms and nanopyramids can be related to their difference in shape, where the different anisotropies, domains, and number of surfaces within the nanocrystals play an essential role in the magnetic properties of the nanoparticles.[40] Although bulk Ni_3S_4 is an antiferromagnet, our result suggests a ferromagnetic behavior for the Ni_3S_4 tetrahedral nanopyramids. In fact, fine particles of an antiferromagnetic material could exhibit magnetic properties such as superparamagnetism and weak ferromagnetism, wherein the permanent magnetic moment can be attributed to an uncompensated number of spins on two sublattices.[41] The frequency dependent of the AC magnetic susceptibility measurements performed on the nanoprism and nanopyramids confirm this conclusion and show a 3D magnetic ordering at 4 and 12 K respectively (Fig. 5c, 5d). The frequency dependence of χ' near the phase transition agrees with the presence of a degree of cluster-glass like behavior with the Mydosh parameter, $\phi = \Delta T_m/T_g/\Delta log$,[42] being estimated as 0.05 and 0.02 for the
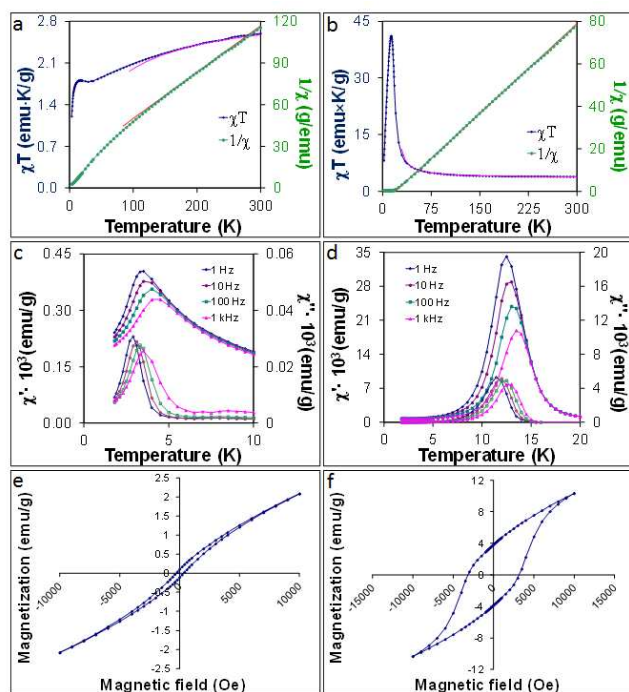
Fig. 5 The temperature dependence of χT ($\lozenge$) and of the inverse susceptibility $1/\chi$ (o) for nanoprism (a) and nanopyramids (b). The solid lines correspond to the best fit the Curie-Weiss law. Temperature dependence of the real χ' (full symbols) and imaginary χ'' (open symbols) components of the AC susceptibility with oscillating field of 5 Oe at different frequencies for nanoprism (c) and nanopyramids (d). Hysteresis loop for nanoprism (e) and nanopyramids (f).

nanoprisms and tetrahedron respectively. Here ΔT_m is the shift of the peak in χ', $log\ \omega$ is the logarithm of the applied frequency, and T_g is freezing temperature. The hysteresis observed at 1.8 K with coercivity at ~250 Oe and 3200 Oe for the nanoprisms and nanopyramids, respectively is depicted in Fig. 5e and 5f. Indeed, Ni_3S_4 nanoparticles were found to exhibit large coercive fields at low temperature, possible due to surface anisotropy.

Conclusions

Here we have demonstrated a facile one-pot colloidal synthesis of two different shaped Ni_3S_4 nanoparticles by varying the Ni precursor used in the synthesis. The employed synthetic method produced highly pure Ni_3S_4 nanoparticles in high yields. The magnetic behavior of the nanoparticles showed dependence on their shapes. Tetrahedral nanopyramids of Ni_3S_4 nanoparticles showed ferromagnetic properties while the Ni_3S_4 nanoprisms showed random antiferromagnetic interactions between magnetic centers.

Acknowledgements

Notes and references

[a] Department of Chemistry, Texas A&M University, PO Box 30012, College Station, TX 77842, USA. E-mail: batteas@chem.tamu.edu
[b] Department of Chemistry and Biochemistry, James Madison University, Harrisonburg, VA 22802, USA.
[c] Microscopy and Imaging Center, Texas A&M University, College Station, TX 77843, USA.
[d] Department of Chemistry and Physics, Fayetteville State University, Fayetteville, NC, 28301, USA.

† Electronic Supplementary Information (ESI) available: Large field of view TEM images and the UV-visible spectra for the nanoprisms and tetrahedrons are showed in Fig. S1−S3. Table SI-1 summarizes the factors affecting the size and shape of the Ni_3S_4 nanoprisms. Animated videos of the 3D-TEM images for the nanoprism and the nanopyramids are also provided. See DOI: 10.1039/b000000x/

‡ These authors contributed equally to this manuscript.

1. Y. Xia, Y. Xiong, B. Lim and S. E. Skrabalak, *Angew. Chem., Int. Ed.*, 2009, **48**, 60-103.
2. A. R. Tao, S. Habas and P. Yang, *Small*, 2008, **4**, 310-325.
3. T. S. Ahmadi, Z. L. Wang, T. C. Green, A. Henglein and M. A. El-Sayed, *Science*, 1996, **272**, 1924-1925.
4. L. M. Falicov and G. A. Somorjai, *P. Natl. Acad. Sci. USA*, 1985, **82**, 2207-2211.
5. B. Lim, M. Jiang, P. H. C. Camargo, E. C. Cho, J. Tao, X. Lu, Y. Zhu and Y. Xia, *Science*, 2009, **324**, 1302-1305.
6. X. Peng, L. Manna, W. Yang, J. Wickham, E. Scher, A. Kadavanich and A. P. Alivisatos, *Nature*, 2000, **404**, 59-61.
7. X. Duan, Y. Huang, Y. Cui, J. Wang and C. M. Lieber, *Nature*, 2001, **409**, 66-69.
8. W. U. Huynh, J. J. Dittmer and A. P. Alivisatos, *Science*, 2002, **295**, 2425-2427.
9. M. Law, L. E. Greene, J. C. Johnson, R. Saykally and P. Yang, *Nat. Mater.*, 2005, **4**, 455-459.
10. J. Xiang, W. Lu, Y. Hu, Y. Wu, H. Yan and C. M. Lieber, *Nature*, 2006, **441**, 489-493.
11. M. H. Huang, S. Mao, H. Feick, H. Yan, Y. Wu, H. Kind, E. Weber, R. Russo and P. Yang, *Science*, 2001, **292**, 1897-1899.
12. X. Duan, Y. Huang, R. Agarwal and C. M. Lieber, *Nature*, 2003, **421**, 241-245.
13. F. Favier, E. C. Walter, M. P. Zach, T. Benter and R. M. Penner, *Science*, 2001, **293**, 2227-2231.
14. M. Law, H. Kind, B. Messer, F. Kim and P. Yang, *Angew. Chem., Int. Ed.*, 2002, **41**, 2405-2408.
15. S.-C. Han, K.-W. Kim, H.-J. Ahn, J.-H. Ahn and J.-Y. Lee, *J. Alloys Compd.*, 2003, **361**, 247-251.
16. W. J. J. Welters, G. Vorbeck, H. W. Zandbergen, J. W. Dehaan, V. H. J. Debeer and R. A. Vansanten, *J. Catal.*, 1994, **150**, 155-169.
17. R. Cid, P. Atanasova, R. L. Cordero, J. M. Palacios and A. L. Agudo, *J. Catal.*, 1999, **182**, 328-338.
18. X. Jiang, Y. Xie, J. Lu, L. Zhu, W. He and Y. Qian, *Adv. Mater.*, 2001, **13**, 1278-1281.
19. R. D. Tilley and D. A. Jefferson, *J. Phys. Chem. B*, 2002, **106**, 10895-10901.
20. A. Ghezelbash, M. B. Sigman and B. A. Korgel, *Nano Lett.*, 2004, **4**, 537-542.
21. Y. Hu, J. Chen, W. Chen, X. Lin and X. Li, *Adv. Mater.*, 2003, **15**, 726-729.
22. L. Zhang, J. C. Yu, M. Mo, L. Wu, Q. Li and K. W. Kwong, *J. Am. Chem. Soc.*, 2004, **126**, 8116-8117.
23. D. Lundquist, *Ark. Kemi.Mineral. Geol.*, 1947, **24A**, 21.
24. G. Kullerud and R. A. Yund, *J. Petrology*, 1962, **3**, 126-175.

25. C. N. R. Rao and K. P. R. Pisharody, *Prog. Solid State Chem.*, 1976, **10, Part 4**, 207-270.
26. A. Manthiram and Y. U. Jeong, *J. Solid State Chem.*, 1999, **147**, 679-681.
5 27. Y. U. Jeong and A. Manthiram, *Inorg. Chem.*, 2000, **40**, 73-77.
28. A. Ghezelbash and B. A. Korgel, *Langmuir*, 2005, **21**, 9451-9456.
29. H. T. Zhang, G. Wu and X. H. Chen, *Mater. Lett.*, 2005, **59**, 3728-3731.
30. X. Chen, Z. Wang, X. Wang, J. Wan, J. Liu and Y. Qian, *Chem.*
10 *Lett.*, 2004, **33**, 1294-1295.
31. C. An, Z. Zhang, X. Chen and Y. Liu, *Mater. Lett.*, 2006, **60**, 3631-3634.
32. A. L. Abdelhady, M. A. Malik, P. O'Brien and F. Tuna, *J. Phys. Chem. C*, 2012, **116**, 2253–2259.
15 33. Q. Liu, Z. Yan, N. L. Henderson, J. C. Bauer, D. W. Goodman, J. D. Batteas and R. E. Schaak, *J. Am. Chem. Soc.*, 2009, **131**, 5720-5721.
34. G. S. Pawley, *J. Appl. Crystallogr.*, 1981, **14**, 357-361.
35. C.-H. Kuo, T.-E. Hua and M. H. Huang, *J. Am. Chem. Soc.*, 2009, **131**, 17871-17878.
20 36. Y. Wang, S. Xie, J. Liu, J. Park, C. Z. Huang and Y. Xia, *Nano Lett.*, 2013, **13**, 2276-2281.
37. L. Roiban, L. Sorbier, C. Pichon, C. Pham-Huu, M. Drillon and O. Ersen, *Nanoscale*, 2012, **4**, 946-954.
38. J. Zhang, Z. Luo, Z. Quan, Y. Wang, A. Kumbhar, D.-M. Smilgies
25 and J. Fang, *Nano Lett.*, 2011, **11**, 2912-2918.
39. Z. Sun, Z. Luo and J. Fang, *ACS Nano*, 2010, **4**, 1821-1828.
40. Y. A. Koksharov, in *Magnetic Nanoparticles*, Wiley-VCH Verlag GmbH & Co. KGaA2009, pp. 197-254.
41. L. Neel, *Low Temperature Physics*, Gordon and Beach, New York,
30 1962.
42. J. A. Mydosh, *Spin Glasses*, Taylor & Francis, London, 1993.